JACS
JOURNAL OF THE AMERICAN CHEMICAL SOCIETY
Article
pubs.acs.org/JACS

An Oxysulfate $Fe_2O(SO_4)_2$ Electrode for Sustainable Li-Based Batteries

Meiling Sun,[†,‡] Gwenaëlle Rousse,[†,§,∥] Artem M. Abakumov,[⊥] Gustaaf Van Tendeloo,[⊥] Moulay-Tahar Sougrati,[#] Matthieu Courty,[‡] Marie-Liesse Doublet,[∥,#] and Jean-Marie Tarascon*[,†,‡,§,∥]

[†]FRE 3677 "Chimie du Solide et Energie", Collège de France, 11 Place Marcelin Berthelot, 75231 Paris Cedex 05, France

[‡]Laboratoire de Réactivité et Chimie des Solides, UMR CNRS 7314, Université de Picardie Jules Verne, 33 rue Saint-Leu, 80039 Amiens Cedex, France

[§]Sorbonne Universités-UPMC Univ Paris 06, 4 Place Jussieu, F-75005 Paris, France

[∥]Réseau sur le Stockage Electrochimique de l'Energie (RS2E), FR CNRS 3459, 80039 Amiens Cedex, France

[⊥]EMAT, University of Antwerp, Groenenborgerlaan 171, B-2020 Antwerp, Belgium

[#]Institut Charles Gerhardt, UMR CNRS 5253, Université Montpellier 2, CC 1502, Place E. Bataillon, 34905 Montpellier Cedex 5, France

Supporting Information

ABSTRACT: High-performing Fe-based electrodes for Li-based batteries are eagerly pursued because of the abundance and environmental benignity of iron, with especially great interest in polyanionic compounds because of their flexibility in tuning the Fe^{3+}/Fe^{2+} redox potential. We report herein the synthesis and structure of a new Fe-based oxysulfate phase, $Fe_2O(SO_4)_2$, made at low temperature from abundant elements, which electrochemically reacts with nearly 1.6 Li atoms at an average voltage of 3.0 V versus Li^+/Li, leading to a sustained reversible capacity of ≈125 mAh/g. The Li insertion−deinsertion process, the first ever reported in any oxysulfate, entails complex phase transformations associated with the position of iron within the FeO_6 octahedra. This finding opens a new path worth exploring in the quest for new positive electrode materials.

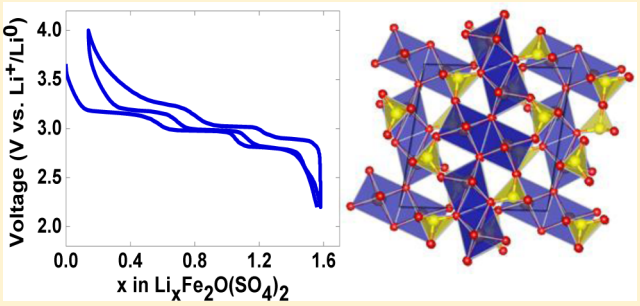

INTRODUCTION

Our planet faces formidable sustainability challenges that call for rigorous and relevant research in various disciplines, including, among others, the field of energy storage and more specifically batteries. Over the past 20 years, Li-ion battery technology has conquered the portable electronics market, has penetrated the electric vehicle (EV) market, and stands as a serious contender for grid applications. Nevertheless, the main issues regarding these large volume applications deal with safety, cost, and sustainability. This calls for innovations at the material level. Great hopes have been placed on Fe-based polyanionic compounds and more specifically $LiFePO_4$,[1] which displays limited capacity because of the weight penalty in replacing an oxygen ion (O^{2-}) with a polyanion $(PO_4)^{3-}$ but offers (i) safety advantages because its redox potential (3.45 V versus Li^+/Li) falls within the thermodynamic stability window of the electrolyte and (ii) sustainability benefits as it is based on abundant Fe and phosphate species.

To increase the Fe^{3+}/Fe^{2+} redox potential and therefore the energy density of polyanionic compounds while preserving their aforementioned positive attributes, researchers have used the inductive effect concept.[2] By replacing $(PO_4)^{3-}$ with the more electronegative $(SO_4)^{2-}$, together with the addition of highly electronegative F^- ion, our group recently succeeded in preparing a new $LiFeSO_4F$ phase that can crystallize either in a *tavorite*[3,4] or a *triplite*[5,6] structure. The latter presents a redox potential of 3.9 V versus Li^+/Li, the highest value ever reported for the Fe^{3+}/Fe^{2+} redox couple in an inorganic compounds. Via further exploitation of the sulfate chemistry, fluorine-free $Li_2Fe(SO_4)_2$[7,8] was isolated, displaying an Fe^{3+}/Fe^{2+} redox potential of 3.83 V versus Li^+/Li. This compound, similar to many other recently discovered Li insertion sulfate compounds ($LiFeSO_4F$, Li_xFeSO_4OH,[9−11] ...), shows polymorphism with a monoclinic and an orthorhombic form,[12,13] both being electrochemically active. Polymorphism also exists in Li-free sulfate compounds as exemplified by $Fe_2(SO_4)_3$ having either a rhombohedral or a monoclinic form,[14,15] the latter being difficult to isolate and showing poor electrochemical performance versus Li.

Although phosphates are less prone to polymorphism, both sulfate and phosphate crystal chemistries bear some resemblance to each other, such as the fluorine-based Li_2FePO_4F[16]/$LiFeSO_4F$ and hydroxide-based Li_2FePO_4OH[17]/$LiFeSO_4OH$

Received: May 30, 2014
Published: August 14, 2014

   dx.doi.org/10.1021/ja505268y | J. Am. Chem. Soc. 2014, 136, 12658−12666

compounds. Additionally, 3d transition metal oxyphosphates and oxysilicates capable of reversibly inserting Li^+ ions are known to form as recently demonstrated by the existence of $LiVOPO_4$[18,19] and Li_2VOSiO_4.[20] Thus, a legitimate course of inquiry was to check the stability of an iron-based oxysulfate insertion compound. An iron oxysulfate is expected to present many appealing aspects. Fundamentally, it sits as a case example to further prove the beneficial inductive effect of sulfate groups. From the application point of view, both the sustainability of iron and sulfates and the lighter molecular weight of oxysulfate compared to those of pure sulfates [e.g., $Fe_2(SO_4)_3$] legitimize the investigation of $Fe_2O(SO_4)_2$.

The literature is rich of thermal analysis and decomposition studies of various iron(II) sulfate hydrates.[21−28] Among these, one previous report[29] indicates the formation of the hydroxysulfate $FeSO_4OH$ occasionally coexisting with another phase, termed the oxysulfate "$Fe_2O(SO_4)_2$", whose respective quantities are defined by the temperature treatment, the gas used to conduct the reaction, and the control of water pressure throughout the reaction. Although the formation of $Fe_2O(SO_4)_2$ can simply be viewed as a result of a condensation−dehydration reaction, several attempts to isolate $Fe_2O(SO_4)_2$ as a pure phase have failed.[30,31] Moreover, suspicions remain regarding this "supposed" compound because different sets of interplanar spacing were reported through the years. This has motivated an impetus to check the real existence of this compound and determine its electrochemical activity versus Li. Herein, we report two ways of preparing powdered samples of $Fe_2O(SO_4)$, determine its crystal structure, and show that this oxysulfate can reversibly take up nearly 1.6 Li atoms per formula unit at an average potential of 3.0 V versus Li^+/Li.

RESULTS

Synthesis. To narrow down the thermal conditions for preparing $Fe_2O(SO_4)_2$, we surveyed the effect of temperature on the thermal stability of $FeSO_4OH$. The hydroxysulfate phase was initially prepared from $FeSO_4{\cdot}7H_2O$ as described by Anji Reddy et al.[9] The commercial heptahydrate Fe(II) sulfate ($FeSO_4{\cdot}7H_2O$, Alfa Aesar, 99%) was first purified to remove traces of Fe^{3+} impurity phases by dissolution in distilled water in the presence of a small amount of ascorbic acid and subsequent precipitation with absolute ethanol and then dried under vacuum at 60 °C. The purified powder was ground in an agate mortar to a fine powder, transferred to an alumina boat, and heated in air at 280 °C for 7 days. The resulting $FeSO_4OH$ powder was parted in several batches and placed in different alumina crucibles, which were all placed in a single oven whose temperature was progressively increased to 440 °C and then maintained at this temperature for 1 day prior to being increased in 5 °C steps to 550 °C. A crucible was removed from the oven at each step of the process to monitor the evolution of the phase's formation through X-ray diffraction (XRD). Figure 1a shows the XRD evolution as a function of temperature. The hydroxysulfate remains the dominant phase up to 445 °C, although a small amount of $Fe_2(SO_4)_3$ is also present at this temperature. Above 450 °C, a new phase, presumably $Fe_2O(SO_4)_2$, appears, coexisting with $Fe_2(SO_4)_3$. The coexistence of the two phases persists up to 475 °C, after which hematite Fe_2O_3 begins to form via the decomposition of $Fe_2(SO_4)_3$, shortly followed by the decomposition of $Fe_2O(SO_4)_2$. This survey led us to conclude that the temperature ranges over which this new phase forms is very narrow.

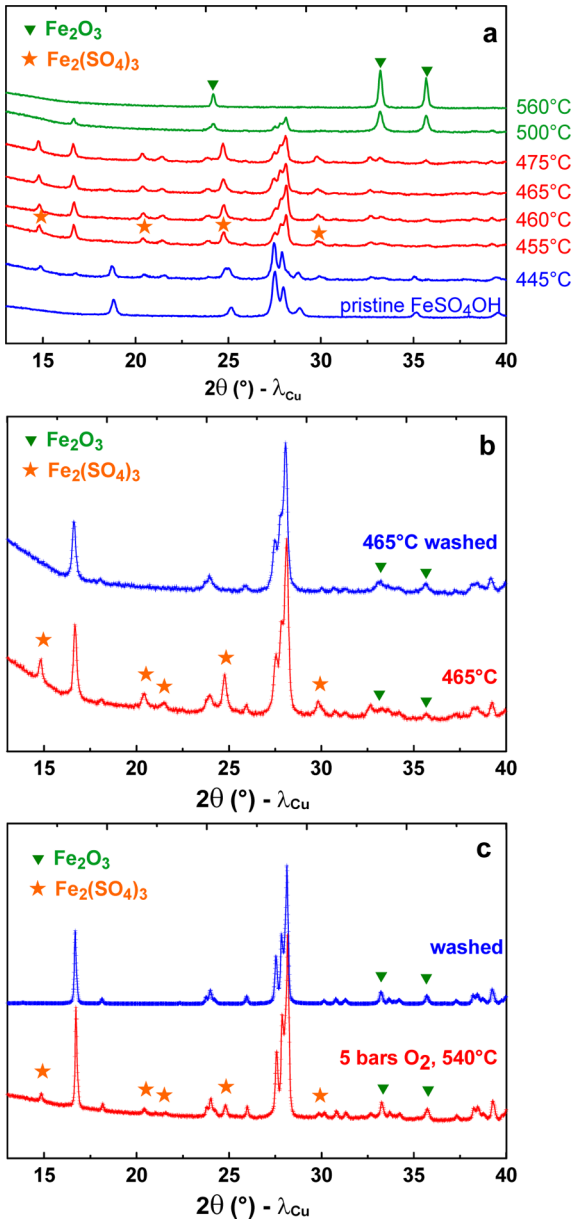

Figure 1. (a) X-ray diffraction patterns of $FeSO_4OH$ heated in air at different temperatures for 72 h. Note the appearance of a definite phase [$Fe_2O(SO_4)_2$] that coexists with $Fe_2(SO_4)_3$ (shown with orange stars) in the narrow range of 455−475 °C. At higher temperatures, this biphasic powder decomposes into hematite Fe_2O_3 (shown with green triangles). (b) Bottom red XRD pattern: mixture of $Fe_2O(SO_4)_2$ and $Fe_2(SO_4)_3$ resulting from the heating of $FeSO_4OH$ at 465 °C. (c) Bottom red XRD pattern: mixture of $Fe_2O(SO_4)_2$ and $Fe_2(SO_4)_3$ obtained by heating $FeSO_4{\cdot}H_2O$ at 540 °C under 5 bar of O_2. For b) and c), the top blue patterns correspond to pure $Fe_2O(SO_4)_2$ obtained after the biphasic powders had been washed with water and ethanol.

On the basis of this knowledge together with the thermogravimetric analysis profile collected by heating $FeSO_4OH$ in air (Figure S1 of the Supporting Information), our best $Fe_2O(SO_4)_2$ sample, containing minimum traces of Fe_2O_3 and $Fe_2(SO_4)_3$, was obtained by keeping $FeSO_4OH$ pellets in a box oven in air at 465 °C for 4 days. As $Fe_2(SO_4)_3$ is water-soluble, the as-prepared powders were washed in water and rinsed with ethanol to produce samples containing a minimum amount of Fe_2O_3 (<10% as determined by

dx.doi.org/10.1021/ja505268y | J. Am. Chem. Soc. 2014, 136, 12658−12666

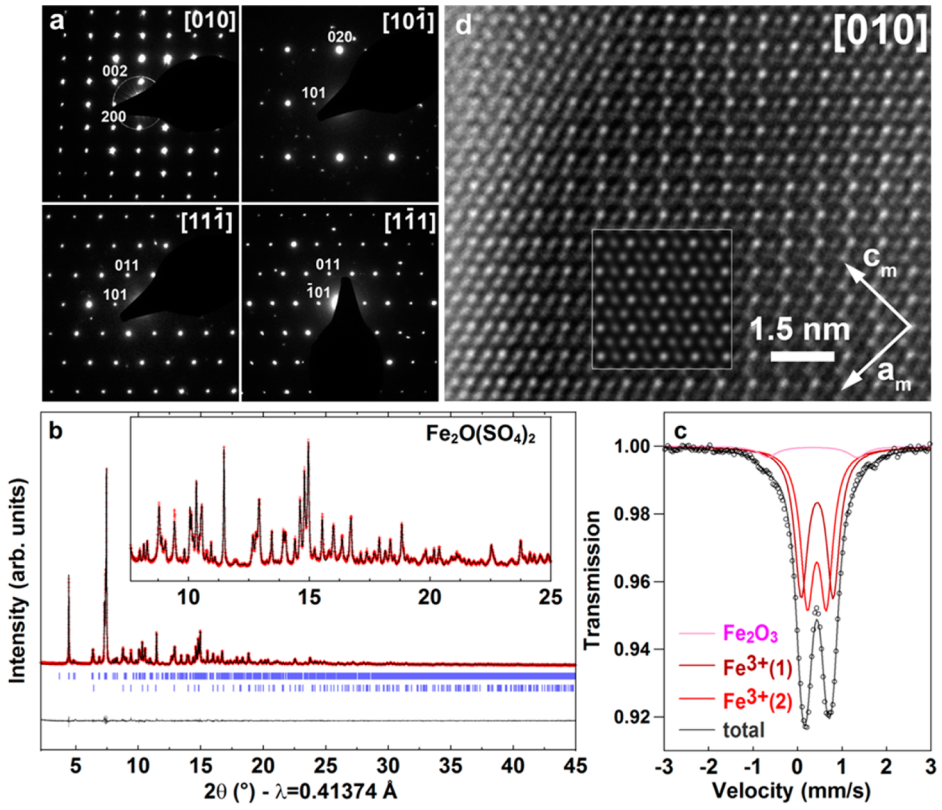

Figure 2. (a) Main SAED patterns of $Fe_2O(SO_4)_2$ indexed on a monoclinic $I2/m$ unit cell. (b) Rietveld refinement of $Fe_2O(SO_4)_2$ against high-resolution X-ray synchrotron powder data (11-BM; λ = 0.41374 Å; R_{Bragg} = 2.93%; χ^2 = 0.93). The red crosses, solid black line, and bottom dark gray line represent the observed, calculated, and difference patterns, respectively. Vertical blue tick bars are the Bragg positions (first line, $Fe_2O(SO_4)_2$; second line, Fe_2O_3). The inset is an enlargement in the 2θ range [8−25°]. (c) Mössbauer spectra of $Fe_2O(SO_4)_2$. The brown and red contributions correspond to the two crystallographically distinct Fe^{3+} atoms in the structure; the pink doublet comes from an ∼10% Fe_2O_3 impurity. (d) [010] HRTEM image of $Fe_2O(SO_4)_2$. The simulated image (defocus d = 6.0 nm; thickness t = 6.4 nm) is shown as an inset.

Mossbauer spectroscopy and Rietveld refinements) (Figure 1b).

Besides the importance of both temperature and annealing times in the growth formation of this new phase, we decided to explore its synthesis in a controlled-pressure environment. Specifically, 50 cm^3 vacuum vessels containing various amounts of $FeSO_4{\cdot}H_2O$ were filled with O_2, with pressures ranging from 1 to 7 bar. The vessel was placed in a vertical tubular furnace and heated at temperatures ranging from 450 to 600 °C for 1−4 days. The cleanest sample, which contained 90 wt % $Fe_2O(SO_4)_2$ with approximately 5 wt % $Fe_2(SO_4)_3$ and 5 wt % of Fe_2O_3 (Figure 1c), was obtained using 1 g of $FeSO_4{\cdot}H_2O$ with an O_2 backfill pressure of 5 bar by heating for 1 day at 540 °C. As before, the sample was washed with water to remove $Fe_2(SO_4)_3$ to obtain a nearly single-phase $Fe_2O(SO_4)_2$. This sample is more crystallized than samples prepared in air as a result of the higher synthesis temperature and was then used to determine the structure. In contrast, because of its simplicity, the previous synthetic path, which occurs at lower temperatures and does not rely on the use of stainless steel pressure vessels, was preferred for preparing large amounts (10−50 g) of materials for electrode preparation and electrochemical testing.

Structural Characterization. The X-ray powder diffraction (XRD) pattern of $Fe_2O(SO_4)_2$ was collected using a Bruker D8 diffractometer with a Cu Kα radiation source ($\lambda_{Cu\text{-}K\alpha1}$ = 1.54056 Å; $\lambda_{Cu\text{-}K\alpha2}$ = 1.54439 Å) and a Lynxeye detector. It presents many peaks (Figure 1b,c), including a tiny one at d = 6.42 Å, with strong overlap among the triplet of reflections visible around 2θ = 28° (d = 3.2 Å); this indicates that the crystallographic unit cell might be large and/or have a low level of symmetry. In such cases, automatic indexing programs (Dicvol,[32] Treor,[33] and others) commonly used to determine possible unit cells give many possibilities, and it is a challenge to find the correct cell.

The $Fe_2O(SO_4)_2$ sample was studied by transmission electron microscopy (TEM) with a Tecnai G^2 electron microscope operated at 200 kV. The TEM image shows that the sample consists of highly agglomerated nanocrystals with sizes ranging from ∼20 to 100 nm (Figure S2 of the Supporting Information). EDX analysis of the nanocrystals indicates the presence of Fe, S, and O. The reciprocal lattice of $Fe_2O(SO_4)_2$ has been reconstructed by taking a series of selected area electron diffraction (SAED) patterns while rotating the crystallite around a selected reciprocal lattice row. All obtained SAED patterns can be indexed in an I-centered monoclinic cell with the following approximate lattice parameters: $a \approx 9.5$ Å, $b \approx 6.1$ Å, $c \approx 9.8$ Å, and $\beta \approx 97°$. The SAED patterns along the main zone axes are shown in Figure 2a. No extra reflection conditions besides those imposed by the I-centering were observed in the ED patterns, suggesting space group $I2/m$ or its acentric subgroups.

This monoclinic cell was then further tested against the 11-BM synchrotron X-ray diffraction pattern (sample in a 0.5 mm diameter capillary; transmission mode; λ = 0.41374 Å), and we found that unit cell parameters of a = 9.71082(8) Å, b = 6.35288(3) Å, c = 9.92501(6) Å, and β = 98.2851(5)° [V =

dx.doi.org/10.1021/ja505268y | J. Am. Chem. Soc. 2014, 136, 12658−12666

Table 1. Structural Parameters for $Fe_2O(SO_4)_2$, Deduced from the Rietveld Refinement of the Synchrotron XRD Pattern[a]

atom	Wyckoff site	x	y	z	B (Å^2)	BVS
Fe1	4*i*	0.80645(14)	0	0.44500(14)	0.53(3)	3.171(19)
Fe2	4*i*	0.55208(14)	0	0.64497(14)	0.54(3)	3.150(17)
S1	4*i*	0.8940(2)	0	0.7633(2)	0.71(4)	6.056(36)
S2	4*i*	0.3330(2)	0	0.8699(2)	0.41(4)	6.161(39)
O1	8*j*	0.3219(4)	−0.1868(5)	0.9492(4)	0.46(7)	2.187(17)
O2	4*i*	0.7453(5)	0	0.7557(4)	1.18(13)	2.143(24)
O3	4*i*	0.2178(6)	0	0.7526(4)	0.82(10)	2.033(20)
O4	4*i*	0.9404(6)	0	0.6208(5)	0.99(11)	1.826(20)
O5	8*j*	0.5481(4)	0.3165(5)	0.6609(3)	0.33(7)	2.073(15)
O6	4*i*	0.6282(6)	0	0.4727(5)	1.06(13)	2.082(19)
O7	4*i*	0.4708(6)	0	0.8196(5)	1.69(13)	1.934(25)

[a]A bond valence sum analysis for each atom is also reported. $Fe_2O(SO_4)_2$, space group $I2/m$. a = 9.71082(8) Å. b = 6.35288(3) Å. c = 9.92501(6) Å. β = 98.2851(5)°. V = 605.901(7) Å^3. Strain parameters, whose S_{hkl} values using Stephens notation,[37] are as follows: S_{400} = 0.281(6), S_{040} = 0.153(7), S_{004} = 0.112(3), S_{220} = 0.278(21), S_{202} = 0.418(15), S_{022} = 0.305(16), S_{121} = 0.34(3), S_{301} = −0.327(12), and S_{103} = −0.076(8).

605.901(7) Å^3; Z = 4] in space group $I2/m$ could perfectly index all peaks, except for the reflections attributed to hematite Fe_2O_3. Note that we did not transform the structure to the standard $C2/m$ setting as this would lead to a β angle significantly different from 90°. The crystal structure of $Fe_2O(SO_4)_2$ was then determined using direct methods with the EXPO software,[34] which revealed the positions of the Fe, S, and O atoms; the obtained structural model was consistent with the expected chemical formula $Fe_2O(SO_4)_2$. The structure was then refined by the Rietveld method[35] using the FullProf[36] program against the synchrotron pattern (Figure 2b), with Fe_2O_3 as a secondary phase. Noting that the peak width was wider than the instrumental broadening, we refined isotropic size parameters (inducing a full width at half-maximum varying as $Y/\cos\theta$), and strain parameters. As the isotropic strain varies as $X \tan\theta$, it can be decoupled from the size parameter Y. The average crystallite size was refined to 616(5) Å. Anisotropic strain parameters, whose S_{hkl} values using Stephens notation[37] are reported in Table 1, indicate some fluctuations of lattice parameters, especially along [100]. The final atomic parameters are listed in Table 1, together with the results of a bond valence sum analysis (BVS) conducted using the Zachariasen formula with the d_0 parameters characterizing cation−anion pairs taken from ref 38. The refinement against laboratory XRD is shown in Figure S3 of the Supporting Information.

Although prolonged electron beam irradiation gradually leads to sample amorphization, the stability of the structure under an electron beam is sufficient for high-resolution TEM (HRTEM) imaging. The [010] HRTEM image in Figure 2d demonstrates a perfectly ordered $Fe_2O(SO_4)_2$ crystal structure. The simulated HRTEM image (inset in Figure 2d; defocus d = 6.0 nm; thickness t = 6.4 nm) reproduces the experimental contrast fairly well, thus validating the refined structure.

Figures 3 and 4 present the refined $Fe_2O(SO_4)_2$ structure. Iron atoms are distributed on two independent crystallographic sites, being octahedrally coordinated with oxygen. These FeO_6 octahedra are edge-shared and create Fe_2O_{10} dimers, which are connected to each other through one oxygen (denoted O6 in Table 1) to form infinite chains running along [100]. These chains are located at [0 $^1/_2$ 0] and [0 0 $^1/_2$] and are connected to each other through regular SO_4 tetrahedral groups.

A closer look at the structure of $Fe_2O(SO_4)_2$ indicates that O6 is the only oxygen atom that is not part of a SO_4 tetrahedron. O6 is 3-fold coordinated by one Fe1 and two Fe2 atoms (Figure 4a). While Fe2 sits at the center of a nearly

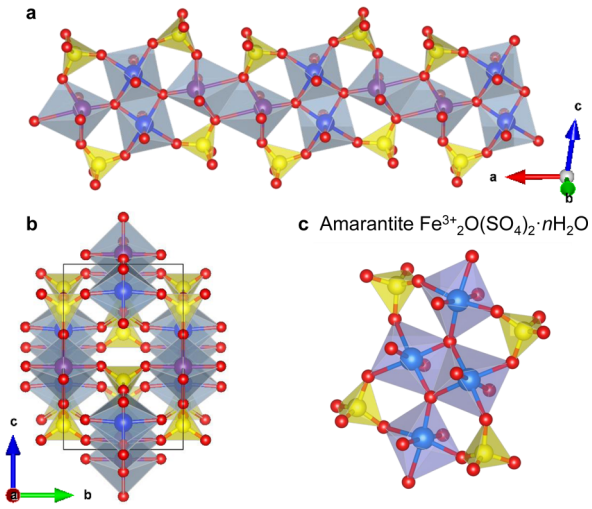

Figure 3. Structure of $Fe_2O(SO_4)_2$ built upon (a) chains of edge- and corner-sharing FeO_6 octahedra running along the [100] direction. (b) View perpendicular to the chains that are linked via SO_4 tetrahedra. Fe1 and Fe2 are shown as purple and blue spheres, respectively. O is colored red and S yellow. (c) Structure of $Fe_2O(SO_4)_2{\cdot}nH_2O$ minerals belonging to the *amarantite* family, drawn with the same color code.

regular octahedron (Fe2−O distances ranging between 1.96 and 2.03 Å), Fe1 clearly appears to be off-center in its octahedron, with one very short (1.79 Å) and one very long (2.63 Å) Fe2−O distance, while the four other distances range between 1.94 and 2.02 Å. This rather uncommon coordination for Fe^{3+} is achieved to satisfy the bond valence sum of O6. To check this further, we examined a model with Fe1 at the center of its coordination octahedron at position (0.8432, 0, 0.43702), i.e., shifted by 0.37 Å from the refined position (0.80645(14), 0, 0.44500(14)). The resulting refinement using this hypothetical structural model is clearly made worse with a bond valence sum of O6 reduced to 1.5, as can be seen from Figure 4b. Note that such short Fe−O distances (1.79 Å) have been reported in other iron-based phosphate and oxyphosphate compounds, specifically $Fe_4(P_2O_7)_3$[39] and $Fe_4(PO_4)_2O$.[40] Similarly distorted FeO_6 octahedra have also been observed in ferrite perovskites $(Pb,Bi)_{1-x}Fe_{1+x}O_{3-y}$ for which the driving force of the off-centering of Fe is attributed to the presence of stereochemically active lone-pair element bismuth or lead.[41,42]

The room-temperature Mössbauer spectrum of the obtained washed powder (Figure 2c) consists of absorption lines with

dx.doi.org/10.1021/ja505268y | J. Am. Chem. Soc. 2014, 136, 12658−12666

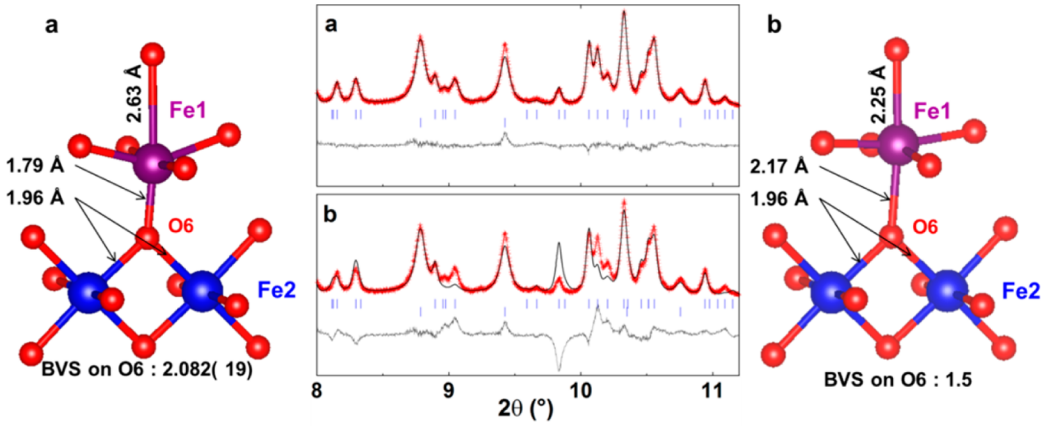

Figure 4. (a) Local arrangement of $Fe_2O(SO_4)_2$ with the off-centering of Fe1 (purple) in its O_6 octahedron. The bond valence sum (BVS) deduced for O6, the oxygen that bridges the three FeO_6 octahedra and is not part of a SO_4 tetrahedron, is displayed. (b) Virtual arrangement with Fe1 placed in the middle of its octahedron and resulting BVS on O6. The middle panel shows the influence of the position of Fe1 on the quality of the refinement of synchrotron powder X-ray diffraction data (11-BM; λ = 0.41374 Å).

average isomer shifts of ~0.4 mm/s, characteristic of high-spin octahedrally coordinated Fe^{3+} cations. Three doublets (i.e., three iron environments) are used to fit the data; the two main components, in equal amounts, present similar isomer shifts (IS of 0.43 and 0.44 mm/s) but different quadrupole splittings (QS) of 0.72 and 0.43 mm/s, attributed to crystallographic sites Fe1 (brown) and Fe2 (red), respectively, on the basis that distorted Fe environments lead to larger QS. The minor doublet (6%, pink) is likely due to residual Fe_2O_3. It is worth noting that, in agreement with XRD, no trace of $Fe_2(SO_4)_3$ can be detected in the Mössbauer spectra.

Electrochemical Characterization. The electrochemical performance of $Fe_2O(SO_4)_2$, ball-milled with 20 wt % carbon black (SP) for 15 min on a Spex-8000 mixer, was evaluated with Swagelok-type cells using a lithium metal disc as a negative electrode, and a Whatman GF/D borosilicate glass fiber sheet saturated with 1 M $LiPF_6$ in ethylene carbonate and dimethyl carbonate [1:1 (w/w)] as the electrolyte. The voltage–composition trace for a Li/$Fe_2O(SO_4)_2$ cell cycled in galvanostatic mode between 2.2 and 4.0 V at a rate of C/40 using a VMP system (Biologic S.A., Claix, France) is shown in Figure 5a. The cell shows electrochemical activity with the ability to reversibly insert more than 1.5 Li atoms per formula unit with limited decay upon cycling (see the inset). This leads to a sustained reversible capacity of approximately 120–125 mAh/g. More precisely, the voltage–composition trace presents a staircase variation with the presence of three well-defined plateaus occurring at ≈3.2, 3.0, and 2.8 V on discharge. Although less pronounced, similar plateaus occur during the subsequent charge sweep and remain upon further cycling. The derivative dx/dV curve (Figure 5b), which contains a series of three sets of redox peaks, highlights the reversibility of these processes. The first set of peaks centered at 2.8 V with a hysteresis of 30 mV and the second set at 3 V without hysteresis are reminiscent of first-order phase transitions, involving two distinct phases. The third set at 3.2 V also seems to indicate a first-order phase transition, but with slow kinetics on oxidation compared to those on reduction.

To understand the mechanism of the Li insertion–extraction process, *in situ* XRD measurements were conducted using a homemade stainless steel cell with an X-ray transparent beryllium window (Figure 6). XRD patterns (λ_{Cu}) were collected every hour for a cell cycled at C/30, i.e., with every

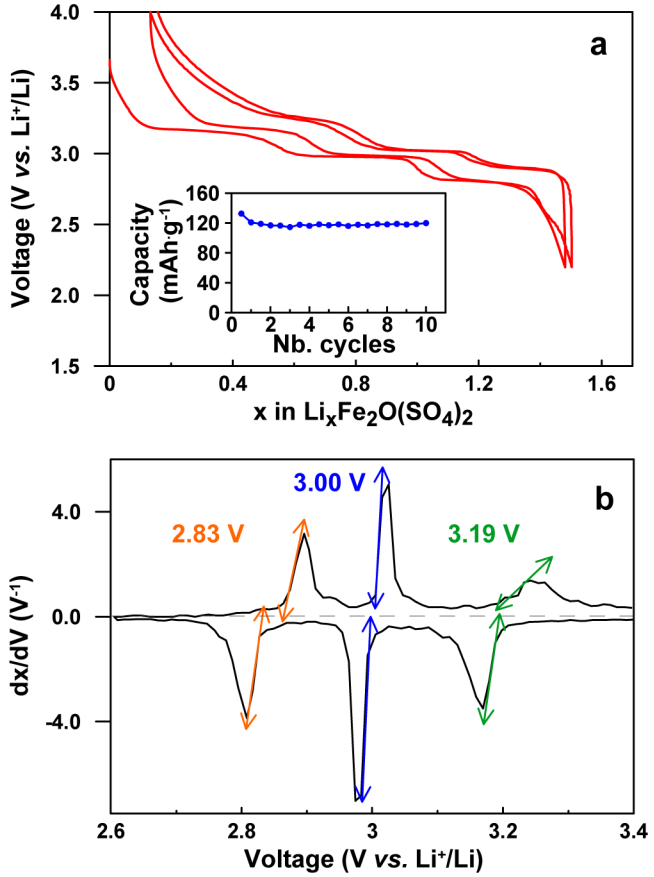

Figure 5. (a) Voltage–composition curve for $Fe_2O(SO_4)_2$. The capacity retention is shown in the inset. (b) Derivative curve dx/dV of the first cycle.

change in lithium stoichiometry of 0.067. During the reduction sweep of the Li/$Fe_2O(SO_4)_2$ cell, we observe a gradual modification of the group of peaks at $2\theta \approx 28°$, which at the end of discharge are well separated. The charging process is reversible, as the pattern at the end of the charge resembles the pattern of the pristine compound.

To analyze the data, we selected the patterns recorded at inflection points between two plateaus in the voltage profile curve because they are usually reminiscent of single-phase

dx.doi.org/10.1021/ja505268y | J. Am. Chem. Soc. 2014, 136, 12658–12666

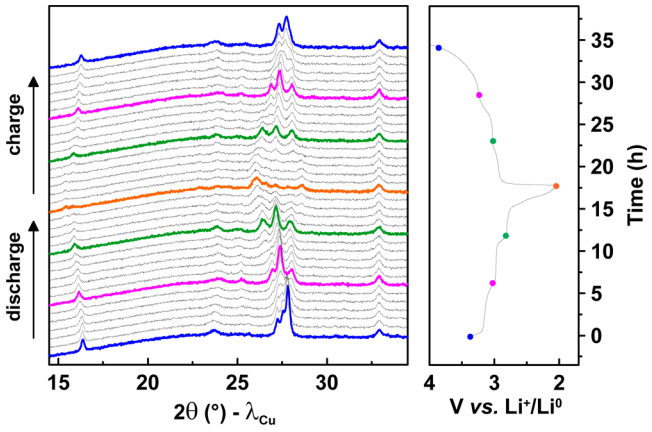

Figure 6. X-ray diffraction patterns recorded *in situ* on the first discharge and subsequent charge. Patterns highlighted in color refer to single-phase compounds, whereas the one colored black correspond to a mixture of phases (biphasic process). The corresponding voltage–time curve is shown at the right. Note the good reversibility of the process.

materials. Single phases $Li_xFe(SO_4)_2$ with $x \approx 0.5$, 1, and 1.5–1.6 (patterns shown in color in Figure 6) were then refined starting with the structural model of the pristine phase but leaving the lattice parameters as variables. Compared to a Le Bail fit, this semi-Rietveld method has the advantage of preventing confusion between overlapping (*hkl*) reflections as intensities of peaks are imposed by the structural model. The refinements are shown in Figure 7 together with the resulting lattice parameters and unit cell volumes. The overall volume change ($\Delta V/V$) is 10% for $Li_{1.6}Fe_2O(SO_4)_2$ compared to 7% for $LiFePO_4$, the most praised material for EV applications. Moreover, we note a sudden decrease in the *a*-axis parameter toward the end of the discharge process to 2.5 V that could be indicative of the total suppression of Fe off-centering beyond threshold Li content, as considered in the Discussion and Conclusions.

We next probed local perturbations in the Fe environments during cycling by performing operando Mössbauer experiments using an electrochemical cell operating in transmission mode. The obtained spectra summarized in Figure 8 indicate a drastic modification of the Mössbauer spectra with increasing Li content. While the pristine material could be fit with two doublets, we now need four doublets denoted (d**1**, d**2**) and (d**3**, d**4**) for Fe^{3+} and Fe^{2+}, respectively, to successfully fit the partially lithiated samples. The Mössbauer study indicates that the insertion process entails three steps, confirming our aforementioned *in situ* X-ray diffraction data.

During the first plateau at ≈3.2 V versus Li^+/Li, both Fe1 and Fe2 of the pristine phase are partially reduced to form two distinct Fe^{2+} sites (denoted d**3** and d**4**, respectively, blue and green). Interestingly, the remaining Fe^{3+} presents a large QS (contribution d**2**, 1.4–1.6 mm/s, colored brown). This partial reduction results in the formation of a new phase that can be written as $Li_x(Fe^{3+})_{2-x}(Fe^{2+})_xO(SO_4)_2$ with $x \sim 0.5$–0.6. Upon further discharge through the second plateau, the amount of Fe^{2+} increases while the remaining Fe^{3+} presents a higher value of QS (1.99 mm/s), indicative of a strongly distorted environment. At the end of the discharge, doublets corresponding to Fe^{3+} are strongly reduced to the benefit of a large Fe^{2+} contribution (d**4**, green). The variations of the total amounts of Fe^{3+} and Fe^{2+} are given in Figure 8. It is worth

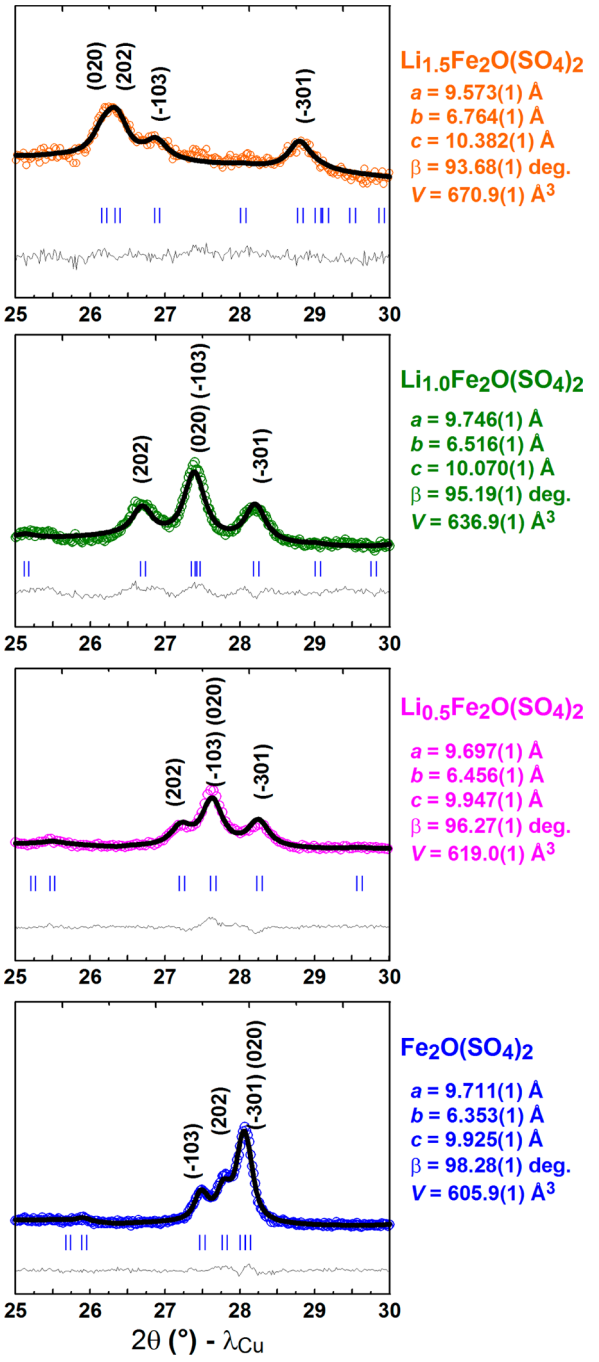

Figure 7. Portion of the semi-Rietveld refinement of three X-ray diffraction patterns collected for pristine $Fe_2O(SO_4)_2$ and at different states of discharge, i.e., $Li_xFe_2O(SO_4)_2$ with $x \approx 0.5$, 1, and 1.5–1.6, which are the patterns corresponding to single-phase compounds. For each composition, lattice parameters and unit cell volumes are indicated.

mentioning that during the first discharge, in agreement with the electrochemical curve, 78% of Fe^{3+} is reduced, with nearly the same amount being oxidized on the following charge, hence confirming the reversibility of the insertion–extraction process as suggested by electrochemical data.

At this stage, a legitimate question involves our inability to electrochemically drive the full lithiation of $Fe_2O(SO_4)_2$ (e.g., reaching a phase with no remaining Fe^{3+}). To address this issue, we first tried to mimic the electrochemical reaction using a mild

dx.doi.org/10.1021/ja505268y | J. Am. Chem. Soc. 2014, 136, 12658–12666

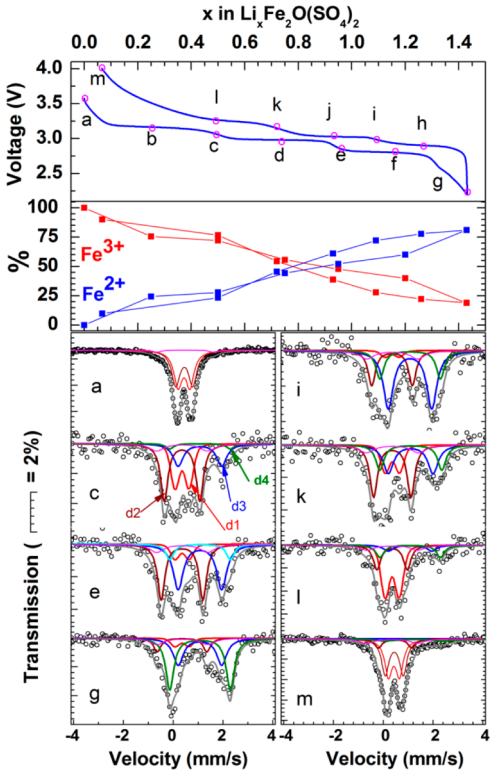

Figure 8. Evolution of the Mössbauer spectra during the first discharge and subsequent charge. The red and brown contributions (d**1** and d**2**, respectively) are from Fe^{3+}, whereas the blue and green contributions (d**3** and d**4**, respectively) present characteristics of Fe^{2+}. The pink contribution comes from the 10% Fe_2O_3 impurity. The total amount of Fe^{2+} and Fe^{3+} is given.

reducing agent such as LiI in acetonitrile (in 5-fold excess). From the lattice parameters [a = 9.708(3) Å, b = 6.487(2) Å, c = 10.058(3) Å, and β = 95.04(1)°] of the obtained "$Li_xFe_2(SO_4)_2$" after reaction for 2 days at room temperature, we could indirectly deduce a Li content of $x \approx 0.8-1.0$, in agreement with atomic absorption measurement and consistent with the limited reducing power of the I^-/I_3^- couple (~2.7 V vs Li/Li$^+$). To increase the amount of incorporated Li ions, we tried stronger reducing agents such as *n*-BuLi (~1.2 V vs Li$^+$/Li); in this case, we observed the production of an amorphous compound, confirming the difficulty of achieving complete lithiation [$Li_2Fe_2O(SO_4)_2$].

DISCUSSION AND CONCLUSIONS

We have reported the existence of the oxysulfate $Fe_2O(SO_4)_2$ and determined its crystal structure in which one the two Fe^{3+} ions is off-centered from its octahedral position. Aside from this peculiar aspect that permits O6 not linked to a sulfate group to fulfill the bond valence sum, it is worth noting that the structure of $Fe_2O(SO_4)_2$ shares similarities with the structures presented in the *amarantite* group,[43−45] which enlist three minerals that differ only by their water content: *hohmannite* $Fe^{3+}{}_2O(SO_4)_2 \cdot 8H_2O$, *amarantite* $Fe^{3+}{}_2O(SO_4)_2 \cdot 7H_2O$, and *metahohmannite* $Fe^{3+}{}_2O(SO_4)_2 \cdot 3H_2O$. These three hydrated iron sulfates are built upon the same unit made of four FeO_6 octahedra, with two of them linked by an edge and the two others connected through vertices as shown in Figure 3c. The same units are present in $Fe_2O(SO_4)_2$ but are condensed so that they form chains. In spite of such a structural resemblance, we did not observe a transformation from $Fe_2O(SO_4)_2$ to any *amarantite*-related mineral when the sample was washed with water. This does not come as a surprise as *hohmannite* is known to be an unstable mineral that transforms into the less hydrated forms *amarantite* and *metahohmannite*. In light of these remarks, an obvious extension of this work is to prepare these minerals to provide an alternative eco-efficient process for the preparation of pure $Fe_2O(SO_4)_2$. Until now, our preliminary attempts to obtain these hydrates as pure phases were unsuccessful.

Previous reports have addressed the thermal decomposition of $FeSO_4 \cdot H_2O$ in oxygen poor or rich atmospheres, with the latter supposedly leading to single-phase $Fe_2O(SO_4)_2$ at 540 °C. Caution must be exercised as none of the reported X-ray diffraction data are similar to the pattern of the $Fe_2O(SO_4)_2$ phase characterized and described herein. Structurally, an examination of the previously published data for $Fe_2O(SO_4)_2$ is consistent with a mixture of most rhombohedral $Fe_2(SO_4)_3$ with the oxysulfate $Fe_2O(SO_4)_2$ as the minority phase (see Figure S4 of the Supporting Information). The peaks are slightly shifted from their expected positions presumably because of angle offsets and/or sample height errors. This is most likely the reason why the authors stated "The results obtained in characterizing $Fe_2O(SO_4)_2$ prove that in its structural, chemical and morphological properties $Fe_2O(SO_4)_2$ is quite similar to $Fe_2(SO_4)_3$".[30] This contrasts with our present findings that $Fe_2O(SO_4)_2$ can be obtained with high purity by washing away $Fe_2(SO_4)_3$, and that this phase exhibits chemical properties distinct from those of $Fe_2(SO_4)_3$. Here, we took advantage of this difference to easily prepare large amounts of $Fe_2O(SO_4)_2$ electrodes.

It nevertheless remains that the previously reported phase differs from $Fe_2O(SO_4)_2$, and we believe that such a difference is nested in the synthesis conditions. Here we have shown that controlling the equilibrium among the $Fe_2(SO_4)_3$, Fe_2O_3, and $Fe_2O(SO_4)_2$ phases is quite tricky. Slight changes in temperature, annealing time, or partial pressure of the oxidative O_2/H_2O gas mixture can result in multiphase samples having different $Fe_2O(SO_4)_2$ contents. This difficulty most likely explains why few oxysulfates including a 3d metal different from iron have so far been reported.[46−50] This is also consistent with a previous report[40] stating that structures having O^{2-} anions coexisting with highly stable polyanions $(XO_4)^{n-}$ are quite unusual and become more rare as the charge of X increases in going from to Si to P and S, hence explaining the large number of oxysilicates reported as compared to the number of oxyphosphates or oxysulfates. Within such types of oxo-based structures, of which $Fe_2O(SO_4)_2$ serves as an excellent example, oxygen atoms that are not part of the $(SO_4)^{2-}$ polyanion but bonded specifically to Fe atoms (such as O6 herein) are relatively labile, explaining why the purely polyanionic $Fe_2(SO_4)_3$ phase is always the phase competing with $Fe_2O(SO_4)_2$. The fact that this oxygen is not part of a SO_4 group (no inductive effect) is also consistent with the lower potential presently obtained.

The achievement of preparing the first anhydrous iron oxysulfate allows us to pioneer the electrochemical behavior toward Li in this family of compounds, which entails a complex Li insertion−deinsertion process as indicated by the staircase profile of the voltage−composition curve. Strikingly, aside from a shift in the potential, the voltage composition curve nearly resembles that recently reported during the insertion of Li into $LiVOPO_4$,[18] containing three successive plateaus associated with phase transformations as vanadium is reduced from +4 to

dx.doi.org/10.1021/ja505268y | J. Am. Chem. Soc. 2014, 136, 12658−12666

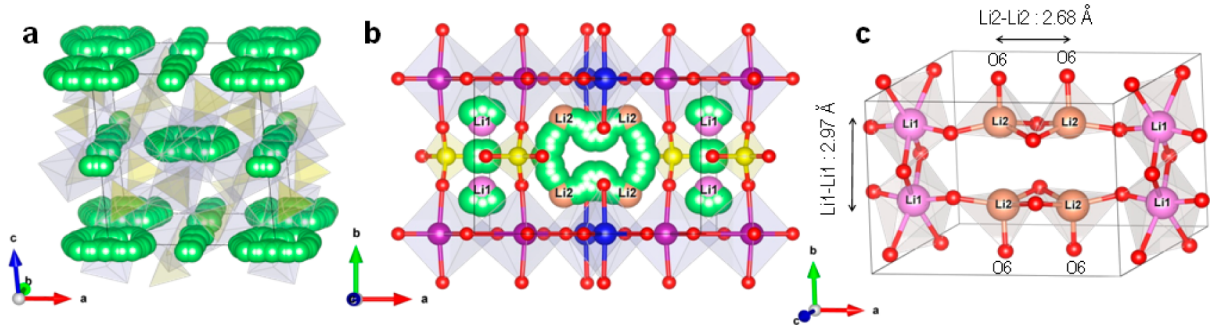

Figure 9. Bond valence sum maps. (a) General view of the unit cell with green spheres corresponding to the positions at which Li would have a BVS sum close to 1. (b) Same unit cell showing the positions of the neighboring FeO_6 octahedra and SO_4 tetrahedra. (c) Coordination of the most probable Li1 and Li2 positions for lithium and resulting Li−Li distances.

+3 (e.g., Li_2VOPO_4). Interestingly, the authors succeeded in determining the crystal structure of $LiVPO_4O$ and Li_2VPO_4O and found a decrease in the vanadium off-centering from the octahedral VO_6 center (e.g., progressive disappearance of the vanadyl-type bonds) as V is reduced from +4 and +3, respectively. Because Fe is off-centered in our pristine material, it could well be that a decrease in Fe off-center displacements takes place as Fe^{3+} is reduced to Fe^{2+}, even though the analogy between V^{4+}−O and Fe^{3+}−O bonding is not straightforward. Neutron diffraction experiments are being planned to check this hypothesis.

The complete reduction of Fe^{3+} to Fe^{2+} would imply an insertion of two lithium ions per formula unit, but experimentally, we could not exceed an insertion of 1.6 Li atoms per formula unit. To gain insight into this issue, we created bond valence maps to assess the possible Li positions in the structure. For this analysis, we considered $Li_{1.6}Fe_2O(SO_4)_2$ with the previously determined cell lattice parameters [a = 9.573(1) Å, b = 6.764(1) Å, c = 10.382(1) Å, and β = 93.68(1)°], but with atomic positions kept as those of the pristine $Fe_2O(SO_4)_2$. The cell was then discretized through a grid of 50 × 50 × 50; a Li is placed on each not, and its bond valence sum is calculated. Figure 9a shows positions within the cell corresponding to a bond valence calculation of +1, which are positions suitable for Li. All possible positions are found at $z \approx 0$ (and $z \approx {}^1/_2$ due to the I-cell-centered unit cell). Among these, two representative positions for lithium, Li1 ($^1/_2$, 0.22, 0) and Li2 (0.14, 0.76, 0) which correspond to the 4h and 8j Wyckoff positions, respectively (Figure 9b), can be considered. The former is six-coordinated with oxygen, while the second is located in a distorted tetrahedral site as highlighted in Figure 9c. The tetrahedral Li environment involves the creation of a Li2−O6 bond that may be associated with the suppression of Fe2 off-centering at the end of discharge. Moreover, it is worthwhile to notice that the distance between Li1 and Li2 is only 2.7 Å, suggesting that electrostatic repulsions could be the origin of our inability to fully lithiate $Fe_2O(SO_4)_2$.

Turning to the redox potential of this electrode, we confirmed its average value of ∼3.0 V by DFT+U calculations, assuming partial (0.5 Li/Fe) and full lithiation (1 Li/Fe). The 8j Wyckoff position, as deduced from the accessible surface area of the nonlithiated starting material, was found as the most probable Li site compared to the 4h Wyckoff position (see Figure S5 and Table 1 of the Supporting Information).

Lastly, in terms of performance, this Li-free $Fe_2O(SO_4)_2$ phase, which can simply be made from abundant elements via a process enlisting a relatively low-temperature step followed by a washing in ethanol, presents an interest for Li metal polymer batteries. It displays a reversible capacity of 125 mAh/g, similar to that of $Fe_2(SO_4)_3$, and is not sensitive to moisture, thus offering a serious asset for electrode processing. In contrast, its voltage is lower because of the weaker inductive effect provided by the number of $(SO_4)^{2-}$ groups per Fe being smaller in $Fe_2O(SO_4)_2$ than in $Fe_2(SO_4)_3$. This new phase shows a lower capacity and potential than $LiFePO_4$ but to its advantage requires neither nanosizing nor nanocoating for proper functioning. Improvements and extensions of this work are immediately apparent and include a broadening of the oxysulfate family by preparing the Mn- and Co-based oxysulfates, which are expected to show redox voltages around 3.55 V (±0.1 V) and 4.05 V (±0.1 V) versus Li, respectively, from DFT+U calculations. Overall, this work provides a solution for stabilizing sulfate-based materials against moisture solubility while offering a new material design path in our quest for new electrode materials.

■ ASSOCIATED CONTENT

Supporting Information

CIF files of $Fe_2O(SO_4)_2$, complementary TGA analysis, X-ray diffraction patterns and Rietveld refinements, TEM image, and DFT calculations. This material is available free of charge via the Internet at http://pubs.acs.org.

■ AUTHOR INFORMATION

Corresponding Author

jean-marie.tarascon@college-de-france.fr

Notes

The authors declare no competing financial interest.

■ ACKNOWLEDGMENTS

We thank N. Recham, M. Ati, J. Rodríguez-Carvajal, J. Kurzman, and M. Reynaud for many fruitful discussions, and R. Janot for expertise in high pressure vessels. Use of the 11-BM mail service of the Advanced Photon Source at Argonne National Laboratory was supported by the U.S. Department of Energy under Contract DE-AC02-06CH11357 and is gratefully acknowledged.

■ REFERENCES

(1) Padhi, A. K.; Nanjundaswamy, K. S.; Goodenough, J. B. *J. Electrochem. Soc.* **1997**, *144*, 1188.

(2) Padhi, A. K.; Manivannan, V.; Goodenough, J. B. *J. Electrochem. Soc.* **1998**, *145*, 1518.

(3) Recham, N.; Chotard, J.-N.; Dupont, L.; Delacourt, C.; Walker, W.; Armand, M.; Tarascon, J.-M. *Nat. Mater.* **2010**, *9*, 68.
(4) Melot, B. C.; Rousse, G.; Chotard, J. N.; Ati, M.; Rodriguez-Carvajal, J.; Kemei, M. C.; Tarascon, J. M. *Chem. Mater.* **2011**, *23*, 2922.
(5) Ati, M.; Melot, B. C.; Chotard, J. N.; Rousse, G.; Reynaud, M.; Tarascon, J. M. *Electrochem. Commun.* **2011**, *13*, 1280.
(6) Barpanda, P.; Ati, M.; Melot, B. C.; Rousse, G.; Chotard, J. N.; Doublet, M. L.; Sougrati, M. T.; Corr, S. A.; Jumas, J. C.; Tarascon, J. M. *Nat. Mater.* **2011**, *10*, 772.
(7) Reynaud, M.; Ati, M.; Melot, B. C.; Sougrati, M. T.; Rousse, G.; Chotard, J.-N.; Tarascon, J.-M. *J. Electrochem. Commun.* **2012**, *21*, 77.
(8) Reynaud, M.; Rousse, G.; Chotard, J. N.; Rodriguez-Carvajal, J.; Tarascon, J. M. *Inorg. Chem.* **2013**, *52*, 10456.
(9) Anji Reddy, M.; Pralong, V.; Caignaert, V.; Varadaraju, U. V.; Raveau, B. *J. Electrochem. Commun.* **2009**, *11*, 1807.
(10) Subban, C. V.; Ati, M.; Rousse, G.; Abakumov, A. M.; Tendeloo, G. V.; Janot, R.; Tarascon, J.-M. *J. Am. Chem. Soc.* **2013**, *135*, 3653.
(11) Ati, M.; Sougrati, M. T.; Rousse, G.; Recham, N.; Doublet, M. L.; Jumas, J. C.; Tarascon, J. M. *Chem. Mater.* **2012**, *24*, 1472.
(12) Lander, L.; Reynaud, M.; Rousse, G.; Sougrati, M. T.; Laberty-Robert, C.; Messinger, R. J.; Deschamps, M.; Tarascon, J.-M. *Chem. Mater.* **2014**, *26*, 4178.
(13) Reynaud, M.; Rodríguez-Carvajal, J.; Chotard, J.-N.; Tarascon, J.-M.; Rousse, G. *Phys. Rev. B* **2014**, *89*, 104419.
(14) Manthiram, A.; Goodenough, J. B. *J. Power Sources* **1989**, *26*, 403.
(15) Nanjundaswamy, K. S.; Padhi, A. K.; Goodenough, J. B.; Okada, S.; Ohtsuka, H.; Arai, H.; Yamaki, J. *Solid State Ionics* **1996**, *92*, 1.
(16) Tarascon, J.-M.; Recham, N.; Armand, M.; Chotard, J.-N.; Barpanda, P.; Waker, W.; Dupont, L. *Chem. Mater.* **2010**, *22*, 724.
(17) Marx, N.; Croguennec, L.; Carlier, D.; Wattiaux, A.; Le Cras, F.; Suard, E.; Delmas, C. *Dalton Trans.* **2010**, *39*, 5108.
(18) Bianchini, M.; Ateba Mba, J.-M.; Dagault, P.; Bogdan, E.; Carlier, D.; Suard, E.; Masquelier, C.; Croguennec, L. *J. Mater. Chem. A* **2014**, *2*, 10182−10192.
(19) Saravanan, K.; Lee, H. S.; Kuezma, M.; Vittal, J. J.; Balaya, P. *J. Mater. Chem.* **2011**, *21*, 10042.
(20) Prakash, A. S.; Rozier, P.; Dupont, L.; Vezin, H.; Sauvage, F.; Tarascon, J. M. *Chem. Mater.* **2006**, *18*, 407.
(21) Bristoti, A.; Kunrath, J. I.; Viccaro, P. J.; Bergter, L. *J. Inorg. Nucl. Chem.* **1975**, *37*, 1149.
(22) Jerman, Z.; Knob, B. *Chem. Prum.* **1973**, *23*, 499.
(23) Kamel, A. H.; Sawires, A.; Khalifa, H.; Saleh, S. A.; Abdellah, A. M. *J. Appl. Chem. Biotechnol.* **1972**, *22*, 591.
(24) Margulius, E. V.; Shokharev, M. M.; Savecheniko, L. A.; Kopylov, N. I.; Beiekeeva, L. I. *Russ. J. Inorg. Chem.* **1971**, *16*, 392.
(25) Neto, K. S.; Garg, V. K. *J. Inorg. Nucl. Chem.* **1975**, *37*, 2287.
(26) Safiullin, N. S.; Gitis, E. B.; Panasenko, N. M. *Russ. J. Appl. Chem.* **1969**, *42*, 1843.
(27) Swamy, M. S. R.; Prasad, T. P. *J. Therm. Anal.* **1980**, *19*, 297.
(28) Swamy, M. S. R.; Prasad, T. P.; Sant, B. R. *J. Therm. Anal.* **1979**, *15*, 307.
(29) Pelovski, Y.; Petkova, V.; Nikolov, S. *Thermochim. Acta* **1996**, *274*, 273.
(30) Petkova, V.; Pelovski, Y. *J. Therm. Anal. Calorim.* **2001**, *64*, 1025.
(31) Swamy, M. S. R.; Prasad, T. P. *J. Therm. Anal.* **1981**, *20*, 107.
(32) Boultif, A.; Louer, D. *J. Appl. Crystallogr.* **1991**, *24*, 987.
(33) Werner, P.-E.; Eriksson, L.; Westdahl, M. *J. Appl. Crystallogr.* **1985**, *18*, 367.
(34) Altomare, A.; Burla, M. C.; Camalli, M.; Carrozzini, B.; Cascarano, G. L.; Giacovazzo, C.; Guagliardi, A.; Moliterni, A. G. G.; Polidori, G.; Rizzi, R. *J. Appl. Crystallogr.* **1999**, *32*, 339.
(35) Rietveld, H. M. *J. Appl. Crystallogr.* **1969**, *2*, 65.
(36) Rodriguez-Carvajal, J. *Physica B* **1993**, *192*, 55.
(37) Stephens, P. W. *J. Appl. Crystallogr.* **1999**, *32*, 281.
(38) Brown, I. D.; Altermatt, D. *Acta Crystallogr.* **1985**, *B41*, 244.
(39) Elbouaanani, L. K.; Malaman, B.; Gérardin, R.; Ijjaali, M. *J. Solid State Chem.* **2002**, *163*, 412.
(40) Bouchdoug, M.; Courtois, A.; Gerardin, R.; Steinmetz, J.; Gleitzer, C. *J. Solid State Chem.* **1982**, *42*, 149.
(41) Abakumov, A. M.; Batuk, D.; Hadermann, J.; Rozova, M. G.; Sheptyakov, D. V.; Tsirlin, A. A.; Niermann, D.; Waschkowski, F.; Hemberger, J.; Van Tendeloo, G.; Antipov, E. V. *Chem. Mater.* **2011**, *23*, 255.
(42) Batuk, D.; Batuk, M.; Abakumov, A. M.; Tsirlin, A. A.; McCammon, C.; Dubrovinsky, L.; Hadermann, J. *J. Inorg. Chem.* **2013**, *52*, 10009.
(43) Scordari, F. *Mineral. Mag.* **1978**, *42*, 144.
(44) Scordari, F.; Ventruti, G.; Gualtieri, A. F. *Am. Mineral.* **2004**, *89*, 265.
(45) Süsse, P. *Z. Kristallogr.—New Cryst. Struct.* **1967**, *54*, 642.
(46) Effenberger, H. *Monatsh. Chem.* **1985**, *116*, 927.
(47) Gatehouse, B. M.; Platts, S. N.; Williams, T. B. *Acta Crystallogr.* **1993**, *B49*, 428.
(48) Kierkegaard, P.; Longo, J. M. *Acta Chem. Scand.* **1965**, *19*, 1906.
(49) Richter, K.-L.; Mattes, R. *Z. Anorg. Allg. Chem.* **1992**, *611*, 158.
(50) Petkova, V.; Pelovski, Y.; Paneva, D.; Mitov, I. *J. Therm. Anal. Calorim.* **2011**, *105*, 793.